Topological Nernst effect emerging from real-space gauge field and thermal fluctuations in a magnetic skyrmion lattice

H. Oike, T. Ebino, T. Koretsune, A. Kikkawa, M. Hirschberger, Y. Taguchi, Y. Tokura, and F. Kagawa

Phys. Rev. B **106**, 214425 — Published 21 December 2022

DOI: 10.1103/PhysRevB.106.214425

Topological Nernst effect emerging from real-space gauge field and thermal fluctuations in a magnetic skyrmion lattice

H. Oike,[1,2,3,*] T. Ebino,[1] T. Koretsune,[4] A. Kikkawa,[3] M. Hirschberger,[1,3] Y. Taguchi,[3] Y. Tokura,[1,3,5] and F. Kagawa[1,3,†]

[1] *Department of Applied Physics and Quantum-Phase Electronics Centre (QPEC), The University of Tokyo, Tokyo 113-8656, Japan*
[2] *PRESTO, Japan Science and Technology Agency (JST), Kawaguchi 332-0012, Japan*
[3] *RIKEN Center for Emergent Matter Science (CEMS), Wako 351-0198, Japan*
[4] *Department of Physics, Tohoku University, Sendai 980-8578, Japan*
[5] *Tokyo College, University of Tokyo, Tokyo 113-8656, Japan*

(Dated: December 6, 2022)

Recent studies on quantum transport in metals have revealed that a gauge field acting on the electron wavefunction yields a peculiar Hall or Nernst effect. When topologically nontrivial spin textures are present, a gauge field appears in real space and affects the electron transport. However, the understanding of the Nernst effect emerging from a real-space gauge filed (topological Nernst effect) remains qualitative, and moreover, the influence of thermal fluctuations has been elusive. Here, we report a pronounced temperature-dependent topological Nernst effect in a metastable skyrmion lattice in MnSi. Our density functional theory assuming a temperature-independent gauge field is successful in an order-of-magnitude estimate of the Nernst signal, whereas the experimental values decrease even significantly with increasing temperature. Similar tendency is also observed for the topological Hall effect, thus indicating that pronounced reduction of the real-space gauge field is crucial for the quantitative understanding of the topological-spin-texture-induced quantum transport at finite temperatures.

I. INTRODUCTION

Recent developments in the Berry phase formalism have revealed a key role of the momentum-space gauge field in understanding transverse electron transport perpendicular to an applied electric field or thermal gradient in metals with broken time-reversal symmetry [1]. When an electron moves in crystal momentum space with constraints on the electronic band structure, it feels a gauge field and acquires the Berry phase depending on its trajectory. Such phase acquisition causes transverse motion of conduction electrons, experimentally manifested in the anomalous Hall and Nernst effects (AHE and ANE, respectively)[1–9]. Analogous Berry phase acquisition may also occur when an electron moves in a topological spin texture matrix with net scalar spin chirality [10–19] . In this case, a gauge field may arise in real space due to the constraint that the conduction electron spin is aligned with the spatially slowly varying local spins, a condition often referred to as the adiabatic limit. In fact, in materials hosting magnetic skyrmions, a topologically nontrivial magnetic texture (Fig. 1(a)), peculiar Hall and Nernst effects were experimentally demonstrated in a magnetic skyrmion lattice (SkL) phase [10–19]. These Hall and Nernst effects are often called the topological Hall effect (THE) and the topological Nernst effect (TNE).

When the THE was first discovered, its understanding was phenomenological [10], but it was later supported microscopically by DFT calculation for the skyrmion-hosting chiral magnet MnSi [13], which exhibits a SkL with moderately long magnetic periodicity, $\lambda_{\mathrm{m}} \approx 19$ nm [20]. To be more specific, however, because DFT calculation for the SkL phase requires impractically high numerical cost, the microscopic approach in the literature was still based on some approximation; namely, it considered the electronic band structure of the ferromagnetic state, instead of the SkL phase, and then calculated the spin-resolved Hall effect under the influence of the effective gauge field. Although this microscopic approach was successful in reproducing the magnitude and the doping dependence of the THE for $Mn_{1-x}Fe_xSi$ at the ground state [13], it is important to test whether the same framework can capture other topological transport phenomena, such as the TNE. However, in MnSi, the TNE has never been reported, and as a matter of fact, no microscopic description based on the spin-resolved band structure has been attempted for a TNE in any skyrmion-hosting material. Thus, observing the TNE as well as the THE in MnSi and comparing the results with DFT calculation would be a stringent test for the microscopic understanding of the topological transport phenomena. As a more nontrivial issue, a finite temperature effect on the real-space gauge field also remains poorly understood. For non-doped MnSi under pressure, for instance, the magnitude of the THE is sensitive to temperature [12–14], but such a finite temperature effect has not been well explained from DFT calculation. Moreover, it is also unclear whether such pronounced temperature dependence is specific to the THE or common to the TNE.

In this Letter, targeting MnSi, we aim to observe the TNE of a skyrmion host in a wide temperature range

* oike@ap.t.u-tokyo.ac.jp
† kagawa@ap.t.u-tokyo.ac.jp

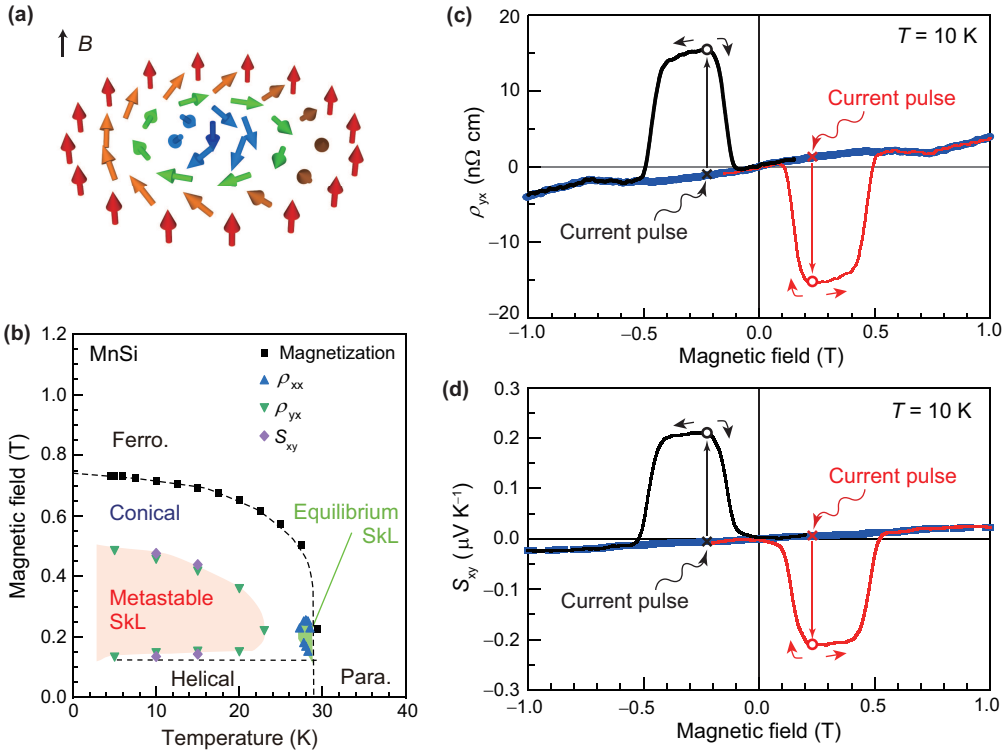

FIG. 1. Large Nernst effect emerging from a metastable skyrmion lattice. (a) Schematic representation of a magnetic skyrmion. (b) Magnetic phase diagram of MnSi. The temperature field region, in which the thermal-quenching-induced metastable skyrmion lattice (SkL) can persist with a prolonged lifetime, is also shown. (c),(d) Magnetic-field dependence of Hall (c) and Nernst (d) signals with/without creating a metastable SkL. Blue curves are the data measured before application of the SkL-creating current pulse to the specimen, whereas the red and balck curves are those after the pulses applied at 0.225 T and −0.225 T, respectively.

and to establish a quantitative description of the TNE in terms of density functional theory (DFT) calculations. In contrast to a previous study [21] that reported the absence of a TNE in a thermodynamically stable SkL phase emergent at 27–29 K, the present study focuses on a metastable SkL that can persist below 23 K down to the lowest temperature [14, 22] (Fig. 1(b)). There are three advantages to studying the metastable SkL. First, the THE signal accompanying the metastable SkL at the lowest temperature is one order of magnitude larger than that accompanying the thermodynamically stable SkL at 27–29 K [14]; therefore, one can expect a large TNE signal for the metastable SkL. Second, one can choose to either create or not create the metastable SkL, potentially leading to ON/OFF tunability of the TNE. As described in the literature [14], on-demand creation of the metastable SkL is possible by performing thermal quenching under 0.20–0.24 T from a high temperature above 29 K to a low temperature. Such thermal quenching is implemented in practice by applying an intense electric current pulse followed by rapid thermal diffusion [14, 23]. Third, the temperature range in that the metastable SkL can exist is wide (0–23 K), thus facilitating the systematic study on the finite temperature effect, which is unknown for the TNE. In this study, we took care to eliminate a potential impact of the experimental procedures on the transport results and therefore performed the Nernst and Hall measurements with the same sample and configuration.

II. RESULTS AND DISCUSSIONS

A. Topological Nernst and Hall effects

A main finding of this study is that a topological Nernst signal accompanies the thermal-quenching-induced metastable SkL with overall behavior quite similar to that of the topological Hall resistivity, ρ_{yx}^{THE} (Figs. 1(c) and 1(d)). Here, let us focus on the Nernst behavior (Fig. 1(d)), S_{xy}, at a low temperature, 10 K, for clarity. The key characteristics are summarized as follows: (i) Without thermal quenching, the SkL does not appear in magnetic field sweeps, and only a vanishingly small Nernst signal, ≈ 0.0 μV K^{-1}, is observed (blue curve in Fig. 1(d)), which is ascribed to the sum of anomalous and ordinary Nernst effects; (ii) after applying a current pulse under 0.225 T, a relatively large Nernst signal, -0.21 μV K^{-1}, emerges as a result of phase conversion, perhaps partial, from a thermodynamically

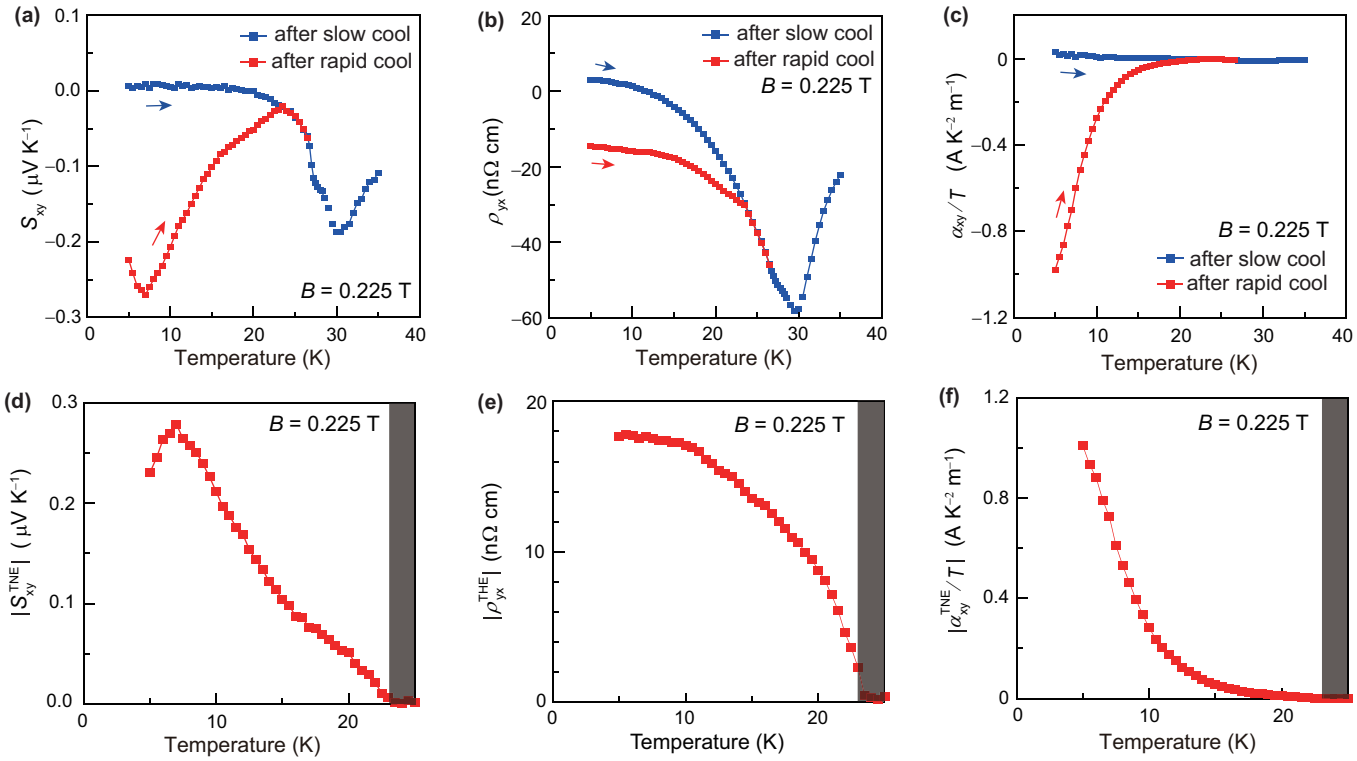

FIG. 2. Temperature dependence of the Nernst and Hall effects emerging from the metastable skyrmion lattice. (a)–(c) Nernst signal S_{xy} (a), Hall resistivity ρ_{yx} (b), and Nernst conductivity divided by temperature α_{xy}/T (c) in the presence/absence of the metastable skyrmion lattice (SkL). Blue curves are the data measured before application of the SkL-creating current pulse to the specimen, whereas the red curves are those after. (d)–(f) Nernst signal (d), Hall resistivity (e), and Nernst conductivity divided by temperature (f) hosted by the metastable SkL. The temperature dependences below 21 K shown in blue or red represent the transport coefficients in the presence or absence of the metastable SkL, respectively. The collapse of the metastable SkL with time is negligible below 21 K, whereas the agreement of the two curves (blue and red) above 23 K is due to collapse of the metastable SkL.

stable conical phase to the metastable SkL; and (iii) the metastable SkL created at 0.225 T (−0.225) is robust against a subsequent field sweep in the range of 0.2–0.4 T (−0.4–−0.2 T), whereas outside this range, it relaxes into topologically trivial magnetic phases, thus resulting in the disappearance of the Nernst signal (red and black curves in Fig. 1(d)). These observations demonstrate that this Nernst signal, unique to the metastable SkL, is identified as the TNE. Our measurements are also successful in detecting a possible TNE signal even for the thermodynamically stable SkL phase at 28 K; however, the magnitude is far smaller, ≈ -0.035 μV K^{-1} (Fig. S1 [23]), suggesting a pronounced temperature dependence of the TNE.

To address the temperature (T) dependence in more detail, comparing S_{xy}–T profiles with and without the SkL is helpful. This approach becomes possible by exploiting the ON/OFF tunability of the metastable SkL. Figure 2(a) displays S_{xy}–T profiles recorded with increasing temperature and a magnetic field of 0.225 T, with and without performing thermal quenching, as represented by red and blue symbols, respectively. The two S_{xy}–T curves are largely different, although the S_{xx}–T profile varies little with the presence or absence of thermal quenching (Fig. S2 [23]). Note that whereas the blue curve tracks the magnetic phases of the thermal equilibrium phase diagram in the absence of the metastable SkL, the red curve is observed in the presence of the metastable SkL up to 23 K. Such cooling-history-dependent behaviors are also observed in the ρ_{yx}–T profiles (Fig. 2(b)). The temperature dependences of the TNE and THE accompanying the metastable SkL is thus derived by subtracting the blue curve from the red curve, as shown in Figs. 2(d) and 2(e), respectively. Although the metastable SkL starts to relax with time into the conical state when the sample temperature reaches 23 K, such a change is negligible below 21 K because of the prolonged lifetime of the metastable SkL ($\gg 10^5$ s) [14]. We thus observe a TNE with a pronounced temperature dependence; its extremal value is ≈ -0.28 μV K^{-1} at 7 K.

Having established the TNE in MnSi and aiming to compare our data to theoretical calculations, we hereafter consider a more intrinsic quantity describing a transverse thermoelectric response, that is, the Nernst conductivity divided by temperature, α_{xy}/T, where α_{xy} is

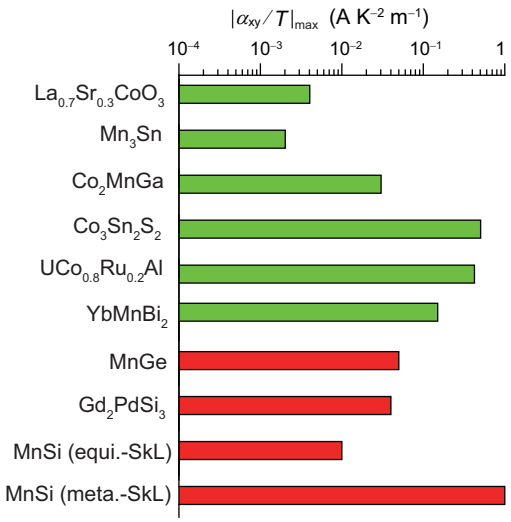

FIG. 3. Comparison of the large Nernst conductivity α_{xy}/T driven by magnetic order for various materials reported in the literature. Green shading indicates an anomalous Nernst response emerging from the momentum-space gauge field [2, 4, 5, 7–9], whereas red shading is the value observed for materials hosting topological magnetic textures [17, 18, 21]. The "equi.-SkL" denotes the thermal equilibrium skyrmion lattice emergent at 27–29 K, whereas the "meta.-SkL" denotes the metastable skyrmion lattice that can persist below 23 K down to the lowest temperature.

given as $\alpha_{xy} = \sigma_{xx}S_{xy} + \sigma_{xy}S_{xx}$. Thus, we present the transverse thermoelectric response in terms of α_{xy}/T in Fig. 2(c), from which the contribution of the metastable SkL to α_{xy}/T (denoted as α_{xy}^{TNE}/T) is derived, as shown in Fig. 2(f). The α_{xy}/T profile in the presence of the metastable SkL (red curve in Fig. 2(c)) is dominated by α_{xy}^{TNE}/T. Its value continuously increases with decreasing temperature and exceeds 1 A K^{-2} m^{-1} at 5 K (Fig. 2(f)). To the best of the authors' knowledge, this is the largest value of α_{xy}/T ever found in magnetic materials.

Comparing the present observations with the α_{xy}/T values for other representative magnets [2, 4, 5, 7–9, 17, 18, 21], as shown in Fig. 3, is instructive. $Co_3Sn_2S_2$, the previous record holder regarding magnetic α_{xy}/T, is a ferromagnetic Weyl semimetal, for which DFT calculation demonstrates a giant ANE originating from the momentum-space gauge field accompanying Weyl points in the electronic structure [7]. Both Gd_2PdSi_3 and MnGe host a topological magnetic texture with a relatively short period of $\lambda_m \approx 3$ nm [19, 24]; Gd_2PdSi_3 is a skyrmion-hosting material similar to MnSi [19], whereas MnGe hosts a three-dimensional spin hedgehog crystal [24]. In these topological magnets, however, a DFT-based microscopic understanding of the THE and TNE has not been attempted, and thus, whether either the real-space or momentum-space gauge field plays a major role in the emergent transverse motion of conduction electrons remains to be determined.

B. DFT calculation

Below, we show how the α_{xy}/T observed in MnSi can be explained microscopically. When considering the real-space gauge field, the adiabatic approximation is often adopted; that is, the associated emergent effective magnetic field, B_{eff}, is given as for the triangular SkL [12, 13], and electrons with majority and minority spins (denoted by $\uparrow$ and $\downarrow$, respectively) feel B_{eff} of opposite sign, causing the transverse motions schematically illustrated in Figs. 4(a) and 4(b). In the literature, the magnitude of ρ_{yx}^{THE} in $Mn_{1-x}Fe_xSi$ was successfully explained with a DFT calculation on the basis of the emergent effective magnetic field in conjunction with the transport coefficients of the collinear ferromagnetic state [13]. To be more specific, the THE was found to be reproduced by the sum of the spin-resolved ordinary Hall effects (OHEs) as

$$\sigma_{xy}^{THE} = \sigma_{xy}^{OHE,\uparrow}(B_{eff}) + \sigma_{xy}^{OHE,\downarrow}(-B_{eff}). \quad (1)$$

Through the present combination of theory and experiment, we aim to clarify whether the experimental TNE can be reproduced by applying the Mott relation to the DFT-calculated energy (ϵ) dependence of $\sigma_{xy}^{THE}(\epsilon, B_{eff})$:

$$\begin{aligned}\frac{\alpha_{xy}^{TNE}}{T} &= \frac{\alpha_{xy}^{ONE,\uparrow}(\epsilon_F, B_{eff}) + \alpha_{xy}^{ONE,\downarrow}(\epsilon_F, -B_{eff})}{T} \\ &= -\frac{\pi^2 k_B^2}{3e}\frac{\partial(\sigma_{xy}^{OHE,\uparrow}(\epsilon, B_{eff}) + \sigma_{xy}^{OHE,\downarrow}(\epsilon, -B_{eff}))}{\partial\epsilon}\bigg|_{\epsilon_F} \\ &= -\frac{\pi^2 k_B^2}{3e}\frac{\partial\sigma_{xy}^{THE}(\epsilon, B_{eff})}{\partial\epsilon}\bigg|_{\epsilon_F}\end{aligned} \quad (2)$$

where k_B and e (> 0) represent the Boltzmann constant and the elementary charge, respectively. Notably, DFT calculations tend to overestimate electron bandwidths in real materials, and the experimental effective mass in MnSi was found to be 5.0±1.2 times larger than the effective mass calculated from DFT [25–27], probably due to strong electron correlation. To compare the calculations and experiments, we therefore renormalize the band energies by a factor of five [23].

From DFT calculations, $\sigma_{xx}^{s}/\tau_s(\epsilon)$ and $\sigma_{xy}^{OHE,s}/B\tau_s(\epsilon)^2$ for the collinear ferromagnetic state are obtained as scattering-independent electronic structure properties (Fig. S3 [23]), where $\tau_s(\epsilon)$ ($s = \uparrow$ or $\downarrow$) is the spin- and energy-dependent relaxation time regarding the crystal momentum. Based on the assumption that $\tau_s(\epsilon) \propto 1/D_s(\epsilon)$, as in a previous study [13], the experimental $\sigma_{xx}(T)$ values (Fig. S2 [23]) were used to obtain $\tau_s(\epsilon, T)$ [23]. The calculated results of $\sigma_{xy}^{OHE,s}(\epsilon, B)/B$ at the lowest temperature, 5 K, are shown in Fig. 4(c). Then, $\alpha_{xy}^{ONE,s}(\epsilon, B)/TB$ at 5 K is derived by assuming the Mott relation, as shown in Fig. 4(d); in this procedure, the energy derivative is increased by the mass enhancement factor [23, 28]. For clarity, the properties for $\epsilon = \epsilon_F$ are

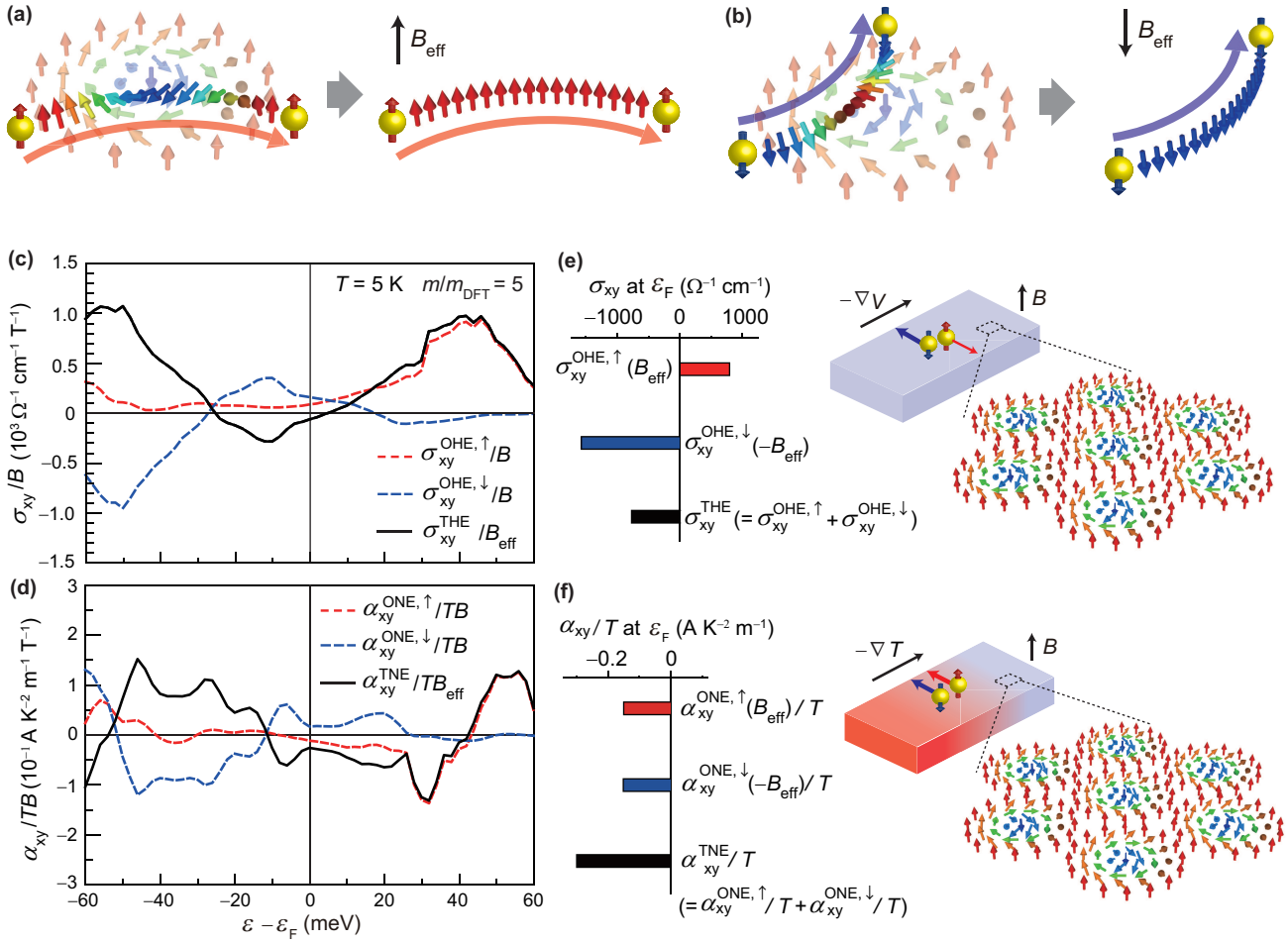

FIG. 4. Estimation of the spin-resolved Nernst conductivity based on first-principles calculations. (a),(b) Schematic trajectories of positively charged particles with majority spin (a) and minority spin (b) passing through a skyrmion texture (left), and corresponding trajectories under the emergent effective magnetic field (right). The arrows represent magnetic moments. The charged particle with majority (minority) spin feels the effective magnetic field in the same (opposite) direction as the applied magnetic field, $B(\parallel z)$. (c),(d) Calculated energy dependence of the spin-resolved ordinary Hall conductivity (c) and ordinary Nernst conductivity divided by temperature (d) in the hypothetical ferromagnetic state. Both values are normalized by the applied magnetic field. (e),(f) Evaluated values of the topological Hall conductivity (e) and topological Nernst conductivity divided by temperature (f), which are expressed as a sum of spin-resolved contributions under the emergent magnetic field of the skyrmion lattice, $B_{\rm eff} \approx 10.5$ T (see text).

displayed in Figs. 4(e) and 4(f), in which we substitute $B_{\rm eff} = 10.5$ T for the metastable SkL with periodicity $\lambda_{\rm m} \approx 22$ nm [22]. When calculating the THE (Fig. 4(e)), $\sigma_{\rm xy}^{\rm OHE,\uparrow}(\epsilon_{\rm F}, B_{\rm eff})$ and $\sigma_{\rm xy}^{\rm OHE,\downarrow}(\epsilon_{\rm F}, -B_{\rm eff})$ exhibit opposite signs, so $\sigma_{\rm xy}^{\rm THE}(\epsilon_{\rm F}, B_{\rm eff})$ is observed as the remnant of the two competing contributions: its calculated value, –790±240 Ω^{-1} cm^{-1}, is on the same order as the experimental value, ≈ –850 Ω^{-1} cm^{-1} (Fig. S2 [23]). Regarding the TNE (Fig. 4(f)), in contrast, $\alpha_{\rm xy}^{\rm ONE,\uparrow}(\epsilon_{\rm F}, B_{\rm eff})/T$ and $\alpha_{\rm xy}^{\rm ONE,\downarrow}(\epsilon_{\rm F}, -B_{\rm eff})/T$ exhibit the same sign and thus additively contribute to $\alpha_{\rm xy}^{\rm TNE}(\epsilon_{\rm F}, B_{\rm eff})/T$, hence giving rise to the giant TNE in MnSi. The calculated $\alpha_{\rm xy}^{\rm TNE}(\epsilon_{\rm F}, B_{\rm eff})/T$ at the base temperature is –0.34±0.11 A K^{-2} m^{-1}, successfully matching the order of magnitude observed in the experiment, ≈ –1 A K^{-2} m^{-1}.

C. Finite temperature effect

Having the success of the quantitative reproduction of the experimental value at the lowest temperature, we also perform the above procedure for other temperatures to gain insight into the pronounced reduction of $\alpha_{\rm xy}^{\rm TNE}/T$ at elevated temperatures. The calculated results are shown in Fig. 5(a), together with the experimental data. Within the temperature range under consideration, the calculated results always have the same order of magnitude

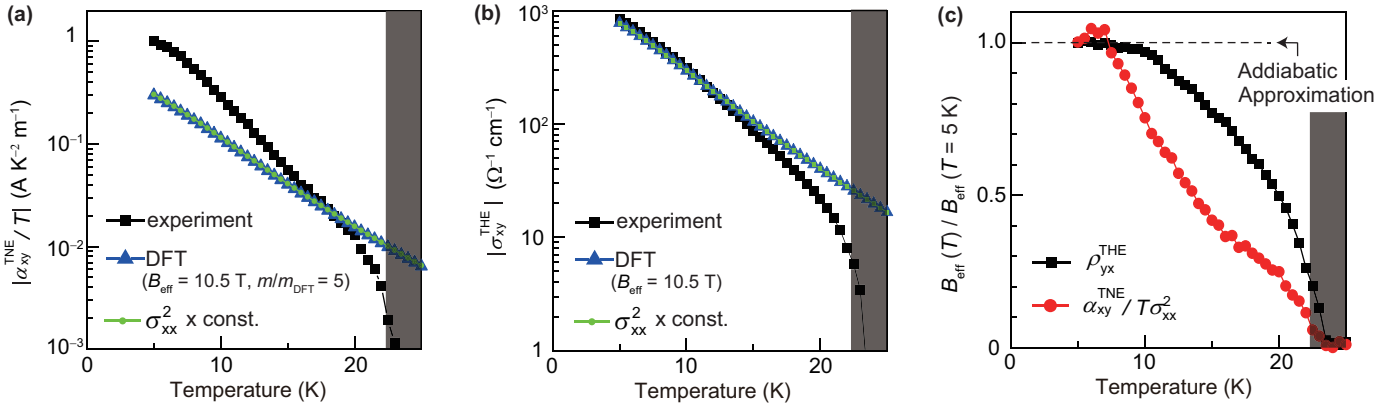

FIG. 5. Finite temperature effects on the topological Nernst and Hall effects and the real-space gauge field. (a),(b) Temperature dependences of the topological Nernst conductivity divided by temperature (a) and topological Hall conductivity (b). The black squares, blue triangles and green circles indicate the experimental results, DFT-based calculation results with a constant effective magnetic field and the square of conductivity σ_{xx} multiplied by a constant value. (c) Temperature dependence of the effective magnetic field normalized at 5 K. The black and red symbols indicate the values of field strength estimated from Hall and Nernst measurements, respectively.

as the experimental results. In the present approach, the temperature dependence of the calculated α_{xy}^{TNE}/T arises exclusively from that of the experimental σ_{xx}, and to be more specific, it is well reproduced by the temperature dependence of σ_{xx}^2 (Fig. 5(a)). This σ_{xx}-sensitive behavior is in sharp contrast to theories and experiments on the ANE related to the momentum-space gauge field: In $UCo_{0.8}Ru_{0.2}Al$ with a large ANE (Fig. 3), for instance, α_{xy}^{ANE}/T depends on σ_{xx} only weakly at low temperatures [8], and a similar behavior is also observed for the ANE in MnSi [21]. Conversely, the observed pronounced temperature dependence of α_{xy}^{TNE}/T corroborates that the Nernst effect unique to the SkL in MnSi originates not from the momentum-space gauge field but from the real-space gauge field.

The experimental temperature dependence of α_{xy}^{TNE}/T is affected mainly by three temperature-dependent factors: (i) the relaxation time, τ; (ii) the band structure, such as the energy splitting between the majority- and minority-spin bands; and (iii) B_{eff} originating from the real-space gauge field. Thus, when one tries to extract a finite temperature effect on B_{eff} from the observed temperature dependence of α_{xy}^{TNE}/T, the other two effects (i) and (ii) should be considered separately. Note that the above DFT calculation neglects the effects (ii) and (iii). Nevertheless, we find within our DFT calculations that even if band structure changes due to temperature-dependent spin polarization in the window of 5–22 K are considered, the calculated TNE and THE do not change so much (Fig. S4 [23]); thus, to the first approximation, we can neglect the effect (ii) as long as the TNE and THE in 5–22 K are considered. Then, to separate the effect (i) from the experimental α_{xy}^{TNE}/T, we referred to the quantity α_{xy}^{TNE}/T divided by σ_{xx}^2 because our DFT calculation has demonstrated that the effect (i) is well captured by considering the temperature-dependent σ_{xx}^2. In this way, the temperature-dependent B_{eff} can be estimated from the TNE. Similarly, the temperature-dependent B_{eff} can also be estimated from the THE. As shown in Fig. 5(b), for the temperature-independent B_{eff}, the temperature dependence of is dominated by that of σ_{xx}^2, a situation in a stark contrast to the momentum-space gauge-field-induced AHE. Thus, by referring to the experimental σ_{xy}^{THE} divided by σ_{xx}^2, which is approximately equal to the experimental ρ_{yx}^{THE}, we estimated the temperature-dependent B_{eff}.

The relative temperature dependence of B_{eff} with respect to the value at the ground state can thus be derived from $\alpha_{xy}^{TNE}/T\sigma_{xx}^2$ and ρ_{yx}^{THE} independently, as shown in Fig. 5(c). Although the two B_{eff}–T profiles do not precisely agree with each other, which is probably partly due to the fact that we neglected the temperature dependence of the band structure, both profiles exhibit the pronounced decrease by almost an order of magnitude with increasing temperature. This overall behavior is independent of whether B_{eff} is estimated from the TNE or THE, and moreover, it has been established that the magnetic periodicity of the SkL varies with temperature only weakly (21.5–21.2 nm for 1.5–20 K) [22]. We therefore conclude that this behavior reflects the intrinsic nature of B_{eff} under the influence of thermal agitations.

Finally, regarding the pronounced attenuation of B_{eff}, we discuss a likely role of spin-angular momentum relaxation. At elevated temperatures, the local magnetic moments consisting of the skyrmion spin texture inevitably fluctuate and change their directions more frequently, rendering the perspective of topology on the skyrmion texture less robust, in particular when a snapshot of the fluctuating spin texture is considered. This obscured spin texture is expected to be also accompanied by enhanced spin-flipping events for moving electrons. Such spin-flip processes are obviously beyond the adiabatic approxima-

tion, which assumes that the conduction electron spin always continuously follows the underlying spin texture as illustrated in Figs. 4(a) and 4(b). Thus, when spin-flip scattering becomes frequent, the effectiveness of Berry phase acquisition should be suppressed compared to the ideal, adiabatic model [29], resulting in a reduced $B_{\rm eff}$. When the temperature is further increased, for instance above 23 K, such frequent spin-flipping events together with the fluctuating spin texture eventually leads to the destruction of the metastable SkL state [14]. Thus, the pronounced attenuation of $B_{\rm eff}$ at elevated temperatures may be referred to as precursor phenomena of the destruction of the topologically protected metastable spin textures.

III. CONCLUDING REMARKS

Our experimental and theoretical studies have revealed that the real-space gauge field derived from the adiabatic approximation can microscopically describe the TNE at the ground state, as long as spin-resolved fermiology, heavy electron mass, and cleanness in terms of electron scattering are appropriately taken into account. On the other hand, at elevated temperatures, the breakdown of the adiabatic approximation should also be considered, which is experimentally manifested as the attenuation of the real-space gauge field. This non-adiabatic effect appears to be crucial when considering the temperature-dependent magnitudes of the THE and TNE unless the considered temperature range is far below the magnetic transition temperature. Topological magnetic textures have been increasingly discovered at various temperatures in recent years [15, 30–32]. Toward the comprehensive understanding of the THE and TNE, it would be important to consider both the real-space gauge field derived from the adiabatic approximation and its attenuation due to the non-adiabatic effect, which is pronounced at elevated temperatures.

In general, electron transport is characterized by fast time scale so that not only thermally averaged but also instantaneous atom and spin configurations can matter. This seems also the case for the THE and TNE. Namely, in addition to the thermally averaged topological structure, it is also crucial to consider instantaneous spin configurations, which potentially includes discontinuities that weaken the validity of physical implications derived from the conventional perspective of topology.

Appendix A: Sample preparation

A single crystal of MnSi was grown by the Czochralski method. The sample size was 1.9 × 0.86 × 0.17 mm^3, with the largest surface normal to the <100> axis. Two terminals for applying a current, four terminals for measuring the voltage and two thermocouples (Spectris Co., Ltd., CHCO-002) were attached to the sample. The sample was placed such that it bridged two sapphire substrates, with one sapphire substrate in thermal contact with a heat bath and the other in thermal contact with a heater.

Appendix B: Resistivity and thermoelectric measurements

The resistivity and Hall resistivity were measured at a current excitation of 17 Hz with the four-probe method under a magnetic field parallel to the <100> axis by means of a lock-in amplifier (NF Corporation, LI5645, or Stanford Research Systems, SR830) equipped with a transformer preamplifier (Stanford Research Systems, SR554). Heat flow to measure the Seebeck and Nernst coefficients was generated by applying a current to the heater, which was in thermal contact with the sample via one of the sapphire substrates. Lock-in measurements were used to improve the signal-to-noise ratio of thermoelectric measurements. By applying an alternating current of 0.3 Hz to the heater, a heat current oscillating at 0.6 Hz was applied to the sample, and thermoelectric voltages were generated in phase with the heat flow. Thermocouple voltages, generated by the temperature gradient in the sample, and thermoelectric voltages were measured by a lock-in amplifier (NF Corporation, LI5645, or Stanford Research Systems, SR830) equipped with a low-noise differential preamplifier (NF Corporation, SA-410F3 or CA-461F2). The thermoelectric coefficients are defined in reference to the generation of an electric field, E, or a current density, j, with respect to an applied temperature gradient as

$$E_i = S_{ij}\partial_j T \tag{B1}$$

$$j_i = \alpha_{ij}\partial_j T \tag{B2}$$

where S and α are the thermoelectric tensor and thermoelectric conductivity tensor, respectively, and (i, $j = x$, y). The relationship between the temperature gradient and the heat flow, $j^{\rm q}$, is given as

$$j_i^{\rm q} = -\kappa_{ij}\partial_j T \tag{B3}$$

where is the thermal conductivity tensor. In the experiments, $j^{\rm q}$ is along the x direction (that is, $j_y^{\rm q} = 0$), and thus,

$$\frac{\partial_y T}{\partial_x T} = -\frac{\kappa_{yx}}{\kappa_{xx}} \tag{B4}$$

Thus, even though $j^{\rm q} \parallel x$, the temperature gradient is not necessarily parallel to the x direction due to the off-diagonal component of κ, or the thermal Hall effect. Consequently, the electric field along the y direction, induced by the heat flow along the x direction, is expressed as

$$E_y = (S_{yx} - S_{yy}\frac{\kappa_{yx}}{\kappa_{xx}})\partial_x T \tag{B5}$$

In the Nernst measurement, the ratio of the temperature gradient in the x direction to the electric field in the y direction is measured, and thus, the Nernst signal N is expressed as

$$\begin{aligned} N &:= -\frac{E_y}{\partial_x T} \\ &= S_{xy} - S_{xx}\frac{\kappa_{xy}}{\kappa_{xx}}, \end{aligned} \tag{B6}$$

where the cubic crystal symmetry of MnSi is taken into account. Although more information on the thermal conductivity tensor is required to determine the exact thermoelectric coefficient, the second term was neglected in the present study, in agreement with previous work (21).

Appendix C: Thermal quenching method

As in previous studies [14, 22], rapid thermal diffusion, which occurs after the direct application of a heat pulse to the sample, was used to thermally quench the crystal. These thermal pulses were generated using Joule heating caused by contact resistance when a current pulse was injected into the sample. The pulse waveform was generated by a voltage output module (National Instruments, NI 9269) and amplified by a high-speed bipolar power supply (NF Corporation, HSA4014) to feed a current of sufficient magnitude (360 mA). A load resistor of 5 ohms was connected in series with the sample to monitor the current flowing through the circuit. The time-varying voltages at the load resistor and at the sample voltage probes were monitored using a voltage input module (National Instruments, NI 9239). Furthermore, the time-varying voltage at the sample voltage probes was amplified with a low-noise differential preamplifier (NF Corporation, CA-461F2). These data on the time variation of the current and voltage were used to determine the time variation of the resistivity of the sample (Fig. S5 [23]). As in the previous study [14], Hall and Nernst signals were confirmed to be cooling rate dependent by varying the fall time of the pulse (Fig. S6 [23]). A switch system (Keithley 7001 equipped with a 7011S) was used to switch the circuit between resistivity/thermoelectric measurements and the pulse-application setup.

Appendix D: DFT calculation

Electronic structure calculations were performed within the generalized gradient approximation [33] in the framework of DFT as implemented in the quantum-ESPRESSO package [34]. Pseudopotentials with the projector augmented wave scheme were used [35]. The size of the magnetic moment was constrained to the experimental value of $M \approx 0.4\mu_{\rm B}$/Mn. Transport properties were calculated using Boltzmann transport theory within the constant relaxation time approximation as in Ref. [13]. The spin-resolved ($s =\uparrow,\downarrow$) conductivity and ordinary Hall conductivity are given as

$$\frac{\sigma^s_{xx}(\epsilon)}{\tau_s(\epsilon)} = \frac{e^2}{VN_k}\sum_{nk}\delta(\epsilon-\epsilon_{nks})(v^x_{nks})^2, \tag{D1}$$

$$\begin{aligned} \frac{\sigma^{{\rm OHE},s}_{xy}(\epsilon,B)}{\tau_s(\epsilon)^2} = \frac{e^3B}{VN_k}\sum_{nk}\delta(\epsilon-\epsilon_{nks})[(v^x_{nks})^2(M^{-1}_{nks})^{yy} \\ -(v^x_{nks})(v^y_{nks})(M^{-1}_{nks})^{xy}] \end{aligned} \tag{D2}$$

Here, V is the unit cell volume, N_k is the number of k points, ϵ_{nks} is the energy of particles in the band with band index n, v_{nks} is the group velocity, and $(M^{-1}_{nks})^{ij} = \partial^2\epsilon_{nks}/(\hbar^2\partial k_i\partial k_j)$ is the inverse effective mass tensor. To calculate these quantities, a Wannier interpolation scheme [36] with a 200 × 200 × 200 k-mesh was employed. When estimating the error in the calculated values, we took into account the error in the Fermi energy position, which is typically ±10 meV. Regarding the effective mass renormalization, see Supplemental Material [23].

ACKNOWLEDGMENTS

H.O. and F.K. thank T. Sato, N. Kanazawa and G. Tatara for their valuable discussions. This work was partially supported by JST PRESTO (Grant No. JPMJPR21Q2), JST CREST (Grant Nos. JPMJCR1874, JPMJCR20T1) and JSPS KAKENHI (Grant Nos. 20K14410, 22H01164, 21H04442).

[1] N. Nagaosa, J. Sinova, S. Onoda, A. H. MacDonald, and N. P. Ong, *Anomalous Hall Effect*, Rev. Mod. Phys. **82**, 1539 (2010).
[2] T. Miyasato, N. Abe, T. Fujii, A. Asamitsu, S. Onoda, Y. Onose, N. Nagaosa, and Y. Tokura, *Crossover Behavior of the Anomalous Hall Effect and Anomalous Nernst Effect in Itinerant Ferromagnets*, Phys. Rev. Lett. **99**, 086602 (2007).
[3] M. Lee, Y. Onose, Y. Tokura, and N. P. Ong, *Hidden Constant in the Anomalous Hall Effect of High-Purity Magnet MnSi*, Phys. Rev. B **75**, 172403 (2007).
[4] M. Ikhlas, T. Tomita, T. Koretsune, M.-T. Suzuki, D. Nishio-Hamane, R. Arita, Y. Otani, and S. Nakatsuji, *Large Anomalous Nernst Effect at Room Temperature in a Chiral Antiferromagnet*, Nature Phys. **13**, 1085 (2017).
[5] A. Sakai, Y. P. Mizuta, A. A. Nugroho, R. Sihombing, T. Koretsune, M.-T. Suzuki, N. Takemori, R. Ishii, D. Nishio-Hamane, R. Arita, *et al.*, *Giant Anomalous Nernst Effect and Quantum-Critical Scaling in a Ferromagnetic Semimetal*, Nature Phys. **14**, 1119 (2018).

[6] M. Mizuguchi and S. Nakatsuji, *Energy-Harvesting Materials Based on the Anomalous Nernst Effect*, Sci. Tech. Adv. Mater. **20**, 262 (2019).

[7] H. Yang, W. You, J. Wang, J. Huang, C. Xi, X. Xu, C. Cao, M. Tian, Z.-A. Xu, J. Dai, *et al.*, *Giant Anomalous Nernst Effect in the Magnetic Weyl Semimetal* $Co_3Sn_2S_2$, Phys. Rev. Mater. **4**, 024202 (2020).

[8] T. Asaba, V. Ivanov, S. Thomas, S. Savrasov, J. Thompson, E. Bauer, and F. Ronning, *Colossal Anomalous Nernst Effect in a Correlated Noncentrosymmetric Kagome Ferromagnet*, Science Adv. **7**, eabf1467 (2021).

[9] Y. Pan, C. Le, B. He, S. J. Watzman, M. Yao, J. Gooth, J. P. Heremans, Y. Sun, and C. Felser, *Giant Anomalous Nernst Signal in the Antiferromagnet* $YbMnBi_2$, Nature Mater. **21**, 203 (2022).

[10] A. Neubauer, C. Pfleiderer, B. Binz, A. Rosch, R. Ritz, P. G. Niklowitz, and P. Böni, *Topological Hall Effect in the A Phase of MnSi*, Phys. Rev. Lett. **102**, 186602 (2009).

[11] N. Nagaosa and Y. Tokura, *Topological Properties and Dynamics of Magnetic Skyrmions*, Nature Nanotech. **8**, 899 (2013).

[12] R. Ritz, M. Halder, C. Franz, A. Bauer, M. Wagner, R. Bamler, A. Rosch, and C. Pfleiderer, *Giant Generic Topological Hall Resistivity of MnSi under Pressure*, Phys. Rev. B **87**, 134424 (2013).

[13] C. Franz, F. Freimuth, A. Bauer, R. Ritz, C. Schnarr, C. Duvinage, T. Adams, S. Blügel, A. Rosch, Y. Mokrousov, *et al.*, *Real-Space and Reciprocal-Space Berry Phases in the Hall Effect of* $Mn_{1-x}Fe_xSi$, Phys. Rev. Lett. **112**, 186601 (2014).

[14] H. Oike, A. Kikkawa, N. Kanazawa, Y. Taguchi, M. Kawasaki, Y. Tokura, and F. Kagawa, *Interplay between Topological and Thermodynamic Stability in a Metastable Magnetic Skyrmion Lattice*, Nature Phys. **12**, 62 (2016).

[15] Y. Tokura and N. Kanazawa, *Magnetic Skyrmion Materials*, Chem. Rev. **121**, 2857 (2020).

[16] Y. P. Mizuta and F. Ishii, *Large Anomalous Nernst Effect in a Skyrmion Crystal*, Sci. Rep. **6**, 1 (2016).

[17] Y. Shiomi, N. Kanazawa, K. Shibata, Y. Onose, and Y. Tokura, *Topological Nernst Effect in a Three-Dimensional Skyrmion-Lattice Phase*, Phys. Rev. B **88**, 064409 (2013).

[18] M. Hirschberger, L. Spitz, T. Nomoto, T. Kurumaji, S. Gao, J. Masell, T. Nakajima, A. Kikkawa, Y. Yamasaki, H. Sagayama, *et al.*, *Topological Nernst Effect of the Two-Dimensional Skyrmion Lattice*, Phys. Rev. Lett. **125**, 076602 (2020).

[19] T. Kurumaji, T. Nakajima, M. Hirschberger, A. Kikkawa, Y. Yamasaki, H. Sagayama, H. Nakao, Y. Taguchi, T.-h. Arima, and Y. Tokura, *Skyrmion Lattice with a Giant Topological Hall Effect in a Frustrated Triangular-Lattice Magnet*, Science **365**, 914 (2019).

[20] S. Mühlbauer, B. Binz, F. Jonietz, C. Pfleiderer, A. Rosch, A. Neubauer, R. Georgii, and P. Böni, *Skyrmion Lattice in a Chiral Magnet*, Science **323**, 915 (2009).

[21] Y. Hirokane, Y. Tomioka, Y. Imai, A. Maeda, and Y. Onose, *Longitudinal and Transverse Thermoelectric Transport in MnSi*, Phys. Rev. B **93**, 014436 (2016).

[22] T. Nakajima, H. Oike, A. Kikkawa, E. P. Gilbert, N. Booth, K. Kakurai, Y. Taguchi, Y. Tokura, F. Kagawa, and T.-h. Arima, *Skyrmion Lattice Structural Transition in MnSi*, Science Adv. **3**, e1602562 (2017).

[23] See Supplemental Material at `http://link.aps.org/supplemental/10.1103/PhysRevX.xxx.xxxxxx` for a detailed description of the experimental and analytical method, and supplementary results.

[24] N. Kanazawa, J.-H. Kim, D. S. Inosov, J. S. White, N. Egetenmeyer, J. L. Gavilano, S. Ishiwata, Y. Onose, T. Arima, B. Keimer, *et al.*, *Possible Skyrmion-Lattice Ground State in the B20 Chiral-Lattice Magnet MnGe as Seen via Small-Angle Neutron Scattering*, Phys. Rev. B **86**, 134425 (2012).

[25] L. Taillefer, G. Lonzarich, and P. Strange, *The Band Magnetism of MnSi*, J. Mag. Mag. Mater. **54**, 957 (1986).

[26] F. P. Mena, D. van der Marel, A. Damascelli, M. Fäth, A. A. Menovsky, and J. A. Mydosh, *Heavy Carriers and non-Drude Optical Conductivity in MnSi*, Phys. Rev. B **67**, 241101(R) (2003).

[27] M. A. Wilde, M. Dodenhöft, A. Niedermayr, A. Bauer, M. M. Hirschmann, K. Alpin, A. P. Schnyder, and C. Pfleiderer, *Symmetry-Enforced Topological Nodal Planes at the Fermi Surface of a Chiral Magnet*, Nature **594**, 374 (2021).

[28] K. Behnia, M.-A. Méasson, and Y. Kopelevich, *Nernst Effect in Semimetals: The Effective Mass and the Figure of Merit*, Phys. Rev. Lett. **98**, 076603 (2007).

[29] K. Nakazawa, M. Bibes, and H. Kohno, *Topological Hall Effect from Strong to Weak Coupling*, J. Phys. Soc. Jpn. **87**, 033705 (2018).

[30] A. K. Nayak, V. Kumar, T. Ma, P. Werner, E. Pippel, R. Sahoo, F. Damay, U. K. Rößler, C. Felser, and S. S. Parkin, *Magnetic Antiskyrmions above Room Temperature in Tetragonal Heusler Materials*, Nature **548**, 561 (2017).

[31] W. Legrand, D. Maccariello, F. Ajejas, S. Collin, A. Vecchiola, K. Bouzehouane, N. Reyren, V. Cros, and A. Fert, *Room-Temperature Stabilization of Antiferromagnetic Skyrmions in Synthetic Antiferromagnets*, Nature Mater. **19**, 34 (2020).

[32] S. Gao, H. Rosales, F. A. Gómez Albarracín, V. Tsurkan, G. Kaur, T. Fennell, P. Steffens, M. Boehm, P. Čermák, A. Schneidewind, *et al.*, *Fractional Antiferromagnetic Skyrmion Lattice Induced by Anisotropic Couplings*, Nature **586**, 37 (2020).

[33] J. P. Perdew, K. Burke, and M. Ernzerhof, *Generalized Gradient Approximation Made Simple*, Phys. Rev. Lett. **77**, 3865 (1996).

[34] P. Giannozzi, S. Baroni, N. Bonini, M. Calandra, R. Car, C. Cavazzoni, D. Ceresoli, G. L. Chiarotti, M. Cococcioni, I. Dabo, *et al.*, *QUANTUM ESPRESSO: a Modular and Open-Source Software Project for Quantum Simulations of Mater.*, J. Phys. Cond. Mat. **21**, 395502 (2009).

[35] P. E. Blöchl, *Projector Augmented-Wave Method*, Phys. Rev. B **50**, 17953 (1994).

[36] G. Pizzi, V. Vitale, R. Arita, S. Blügel, F. Freimuth, G. Géranton, M. Gibertini, D. Gresch, C. Johnson, T. Koretsune, *et al.*, *Wannier90 as a Community Code: New Features and Applications*, J. Phys. Cond. Mat. **32**, 165902 (2020).